Inverse Problems **26** (2010) 025010 (23pp) doi:10.1088/0266-5611/26/2/025010

Eigenfunction contrast source inversion for circular metallic enclosures

Puyan Mojabi and Joe LoVetri

Department of Electrical and Computer Engineering, University of Manitoba, Winnipeg, Manitoba, R3T 5V6, Canada

E-mail: Joe_LoVetri@umanitoba.ca

Received 29 June 2009, in final form 20 November 2009
Published 12 January 2010
Online at stacks.iop.org/IP/26/025010

Abstract

The microwave imaging problem is considered where an object of interest is surrounded by a circular metallic enclosure. A new contrast source inversion (CSI) algorithm which uses eigenfunction expansions of the unknowns is presented for the reconstruction of the complex dielectric profile. Orthonormal eigenfunction expansions associated with the Helmholtz operator for a homogeneous medium and Dirichlet boundary conditions are used for the unknown contrast source and the contrast functions in the CSI functional. These are also used to express the incident field, which is assumed known, as well as for expanding the inverse Helmholtz operator in the CSI functional. The imaging domain is taken to be the whole interior of the metallic enclosure. No prior information, other than keeping the permittivity profile physical, is used. Results are provided for synthetic as well as experimental data. Based on the number of eigenfunctions used, a theoretical limit to the reconstruction quality is defined. Normalized errors relative to this theoretical limit are provided for each of the synthetic data sets.

(Some figures in this article are in colour only in the electronic version)

1. Introduction

In microwave imaging (MWI), one attempts to infer the shape, location and dielectric properties of an object of interest (OI) using microwave measurements collected outside the OI. The inverse problem associated with MWI is nonlinear and ill-posed. Although the new algorithm described herein is applicable to any inverse problem that can be formulated as a boundary value problem for the Helmholtz operator, we are currently developing algorithms and experimental prototypes for electromagnetic-based imaging at microwave frequencies for biomedical applications such as the ones reported in [1–4]. In most microwave imaging systems that have been developed for such applications [3, 5–8] the OI and the antennas

(i.e. field probes) are contained within an enclosed chamber made from a dielectric material such as Plexiglas. The chamber is used to contain a matching fluid to improve the coupling of the microwave energy into the OI. Most of the MWI algorithms used to invert data from these systems assume that the matching fluid extends to infinity, not to the boundary of the casing. This approximation is adequate when the losses of the matching medium are sufficiently large that little or no energy that reaches the boundary of the chamber makes it back to the antennas. To make such an approximation work, the antennas need to be placed close to the OI and away from the boundary, or they need to be directive antennas that direct the main energy towards the OI (e.g. an open-ended waveguide approach).

Recently, researchers have considered the MWI problem when the chamber surrounding the antennas and the OI is made of metallic material (e.g. we use a stainless steel chamber). Various potential advantages of using a conductive chamber with a *lossless* matching medium include advantages related to the inversion algorithms which must be used for these systems as well as to practical data collection advantages such as better signal-to-noise ratios (SNR) [9–11]. The latter is particularly important as it has been suggested in [12, 13] that the true resolution limit for MWI is governed by the achievable SNR of the measurements and not the wavelength. To invert the microwave measurements collected inside a metallic enclosure, researchers have implemented different algorithms which take the metallic casing into account. In [14], a calibration technique was proposed which when applied to the measured data collected inside a circular metallic enclosure allows it to be used by standard inversion algorithms that assume an unbounded matching medium. The proposed calibration technique is based on the reciprocity of the fields inside a circular metallic enclosure and those in an open-space system. It is currently unclear whether such a calibration procedure removes information from the data. In [15], a quasi-Newton inversion algorithm in conjunction with an embedding technique has been used to take into account the circular metallic enclosure. An integral equation formulation of the multiplicative regularized contrast source inversion (MR-CSI) method was used in [10] that uses the Green's function of the metallic cavity. An inversion algorithm, based on conjugate gradient (CG) minimization in conjunction with the finite element method (FEM) forward solver was used in [16]. A Gauss–Newton inversion algorithm with a FEM forward solver to calculate the Jacobian matrix was used in [11] to invert the data collected in conducting cylinders of arbitrary shapes. To the best of our knowledge, all of these inversion algorithms have been applied only to synthetically collected data.

More recently, an inversion algorithm, based on the CG algorithm and a Zernike polynomial representation of the unknown dielectric properties of the OI, was tested against experimentally collected data from the MWI system currently under development at the Institut Fresnel [17]. This system operates at 434 MHz and is enclosed by a circular metallic casing of radius 27.6 cm. In addition, the role of different design parameters in MWI systems with electrically conducting enclosures has been studied in [9] through the singular value expansion of the integral operator mapping the contrast sources inside the OI to the measurement domain outside the OI.

In this paper, we introduce a new method of solving the contrast source inversion (CSI) formulation of the electromagnetic inverse problem using the spectral decomposition of the appropriate boundary value problem applicable to the conductive enclosure MWI setup. From a mathematical perspective, one immediate advantage of using a conductive enclosure setup is that the associated boundary value problem for the electric field is well approximated by the Helmholtz operator in a finite domain which is terminated by perfect electric conductor (PEC) boundary conditions (i.e. homogeneous Dirichlet boundary conditions). This boundary value problem has a discrete set of eigenvalues, i.e. a discrete spectrum, with a complete set of eigenfunctions that is usually used to expand the electromagnetic field within the domain.

Thus, the Helmholtz operator applied to the field represented as an eigenfunction expansion can be replaced by a corresponding eigenfunction expansion where the corresponding eigenvalue replaces the operator operating on each eigenfunction in the expansion. Similarly, the inverse Helmholtz operator for such a boundary value problem has the same eigenfunctions but with eigenvalues that are the reciprocal of those for the forward operator. In the CSI functional defined for the electromagnetic inverse problem the inverse Helmholtz operator is applied to the so-called contrast sources, defined to be the product of the total field and the contrast [2, 18–20]. Taking advantage of the well-known spectral decomposition of the Helmholtz operator within a circular boundary supporting homogeneous Dirichlet boundary conditions, we herein introduce the appropriate eigenfunction expansions for the unknowns in the CSI method, the contrast and the contrast sources. This effectively discretizes all the operators in the CSI functional with the result that the optimization problem becomes one of minimizing the CSI functional over the coefficients of these eigenfunction expansions. One unique result of using the eigenfunction expansion for the unknowns is that the imaging domain becomes the whole interior domain of the conductive enclosure. This is in contrast to the traditional form of the CSI algorithm where the unknown contrast is discretized into pulse basis functions. Inversion results are shown for synthetically collected data sets as well as for preliminary experimental data collected from a conductive enclosure prototype being developed at the University of Manitoba. The experimental results are preliminary in that no well-established techniques are currently available for the calibration of data obtained from within conductive enclosure setups; we simply use the same calibration techniques that have been used by other researchers for open-region setups.

2. Problem statement and notation

Throughout our analysis, we assume a time-harmonic dependence $\exp(-jwt)$ where ω and t represent the angular frequency and time, respectively, and $j^2 = -1$. All the materials considered herein are assumed to be nonmagnetic: the permeability is taken to be that of free-space, μ_0. We consider a PEC enclosure with boundary denoted as Γ of circular cross-section having radius a. The interior volume of the enclosure is denoted by $\mathcal{D}$ which will also denote the imaging domain. The formulation is given for 2D fields; thus, we assume that the domain $\mathcal{D}$ is located in the x–y plane. Inside the enclosure, which will contain the OI, we assume a known homogeneous background medium having a, possibly complex, relative permittivity ϵ_b. The geometrical model of the microwave imaging system is shown in figure 1. The complex electric contrast function $\chi : \mathcal{D} \to \mathbb{C}$, which represents the OI, is defined as

$$\chi(\boldsymbol{r}) = \frac{\epsilon(\boldsymbol{r}) - \epsilon_b}{\epsilon_b} \tag{1}$$

where $\epsilon(\boldsymbol{r})$ is the relative complex permittivity of the OI at the point $\boldsymbol{r} \in \mathcal{D}$.

In what follows, we assume a 2D transverse magnetic (TM) model where the electric field is represented by the single longitudinal component $\boldsymbol{E} = E\hat{z}$. Thus, we refer to the electric field by its scalar component E. The physics of the problem can be modeled using various forms of the Helmholtz equation for E. To aid in the formulation we define the Helmholtz differential operator in a homogeneous background medium, $\mathcal{H}_b : L^2(\mathcal{D}) \to L^2(\mathcal{D})$, as

$$\mathcal{H}_b(\zeta) \triangleq \nabla^2\zeta(\boldsymbol{r}) + k_b^2\zeta(\boldsymbol{r}) \tag{2}$$

where $k_b = \omega\sqrt{\mu_0\epsilon_0\epsilon_b}$ is the wavenumber of the background medium and ∇^2 denotes the Laplacian operator with respect to the coordinate $\boldsymbol{r}$.

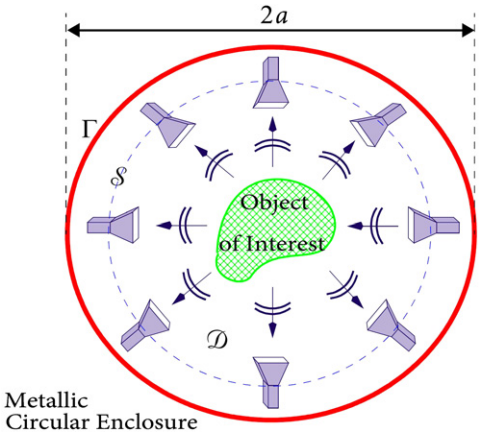

Figure 1. Microwave imaging system enclosed by a circular PEC enclosure Γ (red circle) of radius a. The cross section of the enclosure, which is the imaging domain, is denoted by $\mathcal{D}$. The measurement domain (blue dotted circle), which is outside the object of interest, is denoted by $\mathcal{S}$.

In the MWI problem considered herein, the OI is successively illuminated by known incident fields E_t^{inc}, $(t = 1, 2, \ldots, T)$. Each incident field is produced by a source function S_t, and the field itself satisfies the inhomogeneous Helmholtz equation

$$\mathcal{H}_b\left(E_t^{\text{inc}}\right) = -S_t(\boldsymbol{r}), \tag{3}$$

with the Dirichlet boundary condition

$$E_t^{\text{inc}}(\boldsymbol{r} \in \Gamma) = 0. \tag{4}$$

When the OI is present, this same source produces what is referred to as the total field E_t. The difference between the total field and the incident field is defined as the scattered field $E_t^{\text{scat}} \triangleq E_t - E_t^{\text{inc}}$. It is easily shown that the scattered field satisfies the same Helmholtz differential equation but with the source function replaced by $k_b^2 \chi(\boldsymbol{r}) E_t(\boldsymbol{r})$. That is, the scattered field satisfies

$$\mathcal{H}_b\left(E_t^{\text{scat}}\right) = -k_b^2 \chi(\boldsymbol{r}) E_t(\boldsymbol{r}), \tag{5}$$

with the same homogeneous boundary condition:

$$E_t^{\text{scat}}(\boldsymbol{r} \in \Gamma) = 0. \tag{6}$$

The inverse problem is defined as that of finding the electric contrast $\chi(\boldsymbol{r})$ from measurement data, which consists of the scattered field on the measurement domain $\mathcal{S}$, located outside the OI. The scattered field data are obtained from appropriately calibrated measurements of the total and incident fields at the same location.

3. The contrast source inversion method

We now give a brief overview of the contrast source inversion (CSI) formulation as applied to the enclosed region inverse problem. The CSI method [2,18–20] casts the MWI problem as an optimization problem over the contrast χ and a new variable called the contrast source w_t, defined as $w_t(\boldsymbol{r}) \triangleq \chi(\boldsymbol{r}) E_t(\boldsymbol{r})$. These variables are solved for iteratively by minimizing the specially formulated CSI functional using the CG method. The CSI functional is formulated

via the inverse operator corresponding to the problem formulation previously described. That is, from (5), the scattered field corresponding to the tth transmitter may be written as

$$E_t^{\text{scat}}(\boldsymbol{r}) = \mathcal{H}_b^{-1}\left(-k_b^2 w_t\right), \tag{7}$$

where $\mathcal{H}_b^{-1}$ denotes the inverse of the Helmholtz operator $\mathcal{H}_b$ and includes the boundary condition $E_t^{\text{scat}}(\boldsymbol{r} \in \Gamma) = 0$.

At the nth iteration of the CSI method, the cost-functional $\mathcal{C}_n : L^2(\mathcal{D}) \times L^2(\mathcal{D})^T \to \mathbb{R}$ is given by [21]

$$\begin{aligned}\mathcal{C}_n(\chi, w_t) &= \mathcal{C}_{\mathcal{S}}(w_t) + \mathcal{C}_{\mathcal{D},n}(\chi, w_t) \\ &= \frac{\sum_t \left\| E_t^{\text{meas}} - \mathcal{M}_{\mathcal{S},t}\mathcal{H}_b^{-1}\left(-k_b^2 w_t\right)\right\|_{\mathcal{S}}^2}{\sum_t \left\| E_t^{\text{meas}}\right\|_{\mathcal{S}}^2} + \frac{\sum_t \left\| \chi E_t^{\text{inc}} - w_t + \chi\mathcal{H}_b^{-1}\left(-k_b^2 w_t\right)\right\|_{\mathcal{D}}^2}{\sum_t \left\| \chi_{n-1} E_t^{\text{inc}}\right\|_{\mathcal{D}}^2}\end{aligned} \tag{8}$$

where E_t^{meas} denotes the measured scattered field and $\mathcal{M}_{\mathcal{S},t}$ represents the characteristic operator which selects the measurement points on $\mathcal{S}$; both corresponding to the tth transmitter. Note that information gathered from different transmitters is incorporated into the functional by summing over the transmitters. The second term of the cost-functional $\mathcal{C}_n$, i.e. $\mathcal{C}_{\mathcal{D},n}$, may be regarded as the Maxwell regularizer [22] which is introduced to handle the ill-posedness of the problem.

The cost-functional $\mathcal{C}_n(\chi, w_t)$ is iteratively minimized via the formation of two interlaced sequences: a sequence of contrast estimates $\{\chi_n\}$ computed in an interlaced fashion with a sequence of contrast source estimates $\{w_{t,n}\}$. That is, at each iteration, each unknown is updated using a single step of the CG algorithm while assuming that the other unknown is constant. Note that the CSI functional is quite general, but a form of the inverse operator $\mathcal{H}_b^{-1}$ which is amenable to mathematical manipulation (e.g. the derivative of functional is required for the implementation of the CG optimization), and which lends itself to efficient and accurate computation is required. There are many ways to formulate this operator which meets these requirements. Integral equation methods and the inverse of finite-difference discretization have been used (see, for example, [18–20] for integral equation formulations in unbounded domains, [21] for a novel use of the inverse of a finite-difference discretization, and [10] for an integral equation formulation applicable to the PEC-enclosed problem).

4. Eigenfunction contrast source inversion

The inverse operator $\mathcal{H}_b^{-1}$ for the PEC-enclosed-region problem can be expressed using the eigenfunction expansion of the boundary-value problem that has been defined. Using polar coordinates $\boldsymbol{r}(\rho, \theta)$, the orthonormal eigenfunctions of $\mathcal{H}_b$ which satisfy the homogeneous Dirichlet boundary condition on Γ ($\rho = a$) may be written as

$$\psi_{mp}(\boldsymbol{r}) = \frac{1}{\sqrt{N_{mp}}} J_m\left(\frac{x_{mp}\rho}{a}\right)\cos(m\theta), \tag{9}$$

$$\varphi_{mp}(\boldsymbol{r}) = \frac{1}{\sqrt{N_{mp}}} J_m\left(\frac{x_{mp}\rho}{a}\right)\sin(m\theta), \tag{10}$$

where x_{mp} represents the pth zero ($p \in \mathbb{N}$) of the mth-order Bessel function of the first kind, J_m where $m \in \mathbb{N} \cup \{0\}$. The normalization constants N_{mp} can be easily calculated as

$$N_{mp} = \begin{cases} \pi a^2 J_{m+1}^2(x_{mp}) & m = 0 \\ \dfrac{\pi a^2}{2} J_{m+1}^2(x_{mp}) & \text{otherwise.} \end{cases} \tag{11}$$

The eigenvalues, each of multiplicity 2, corresponding to ψ_{mp} and φ_{mp} are

$$\lambda_{mp} = k_b^2 - \left(\frac{x_{mp}}{a}\right)^2. \tag{12}$$

The completeness of the eigenfunctions allows us to express both the contrast, $\chi(\boldsymbol{r})$, and the contrast source functions, $w_t(\boldsymbol{r})$, inside the bounded domain $\mathcal{D}$ as eigenfunction expansions:

$$\chi(\boldsymbol{r}) = \sum_{m,p} \gamma_{mp}\psi_{mp}(\boldsymbol{r}) + \mu_{mp}\varphi_{mp}(\boldsymbol{r}) \tag{13}$$

and

$$w_t(\boldsymbol{r}) = \sum_{m,p} \alpha_{mp,t}\psi_{mp}(\boldsymbol{r}) + \beta_{mp,t}\varphi_{m,p}(\boldsymbol{r}) \tag{14}$$

where γ_{mp}, μ_{mp}, $\alpha_{mp,t}$ and $\beta_{mp,t}$ are the unknown coefficients to be determined. Note that a double summation is required for these eigenfunction expansions, as compared to the single summation used in the singular value expansion given by [9] and the Zernike expansion used by [17].

A useful property of the eigenfunctions ψ_{mp} and φ_{mp} for the operator $\mathcal{H}_b$ is that they are also the eigenfunctions of the inverse operator $\mathcal{H}_b^{-1}$, but the corresponding eigenvalues for the eigenfunctions of $\mathcal{H}_b^{-1}$ are λ_{mp}^{-1}. Using this property, along with (14), allows us to express (7) as

$$E_t^{\text{scat}}(\boldsymbol{r}) = \mathcal{H}_b^{-1}\left(-k_b^2 w_t\right) = -k_b^2 \sum_{m,p} \lambda_{mp}^{-1}[\alpha_{mp,t}\psi_{mp}(\boldsymbol{r}) + \beta_{mp,t}\varphi_{mp}(\boldsymbol{r})], \tag{15}$$

and the scattered field on the measurement domain as

$$\begin{aligned} E_t^{\text{scat}}(\boldsymbol{r} \in \mathcal{S}) &= \mathcal{M}_{\mathcal{S},t}\mathcal{H}_b^{-1}\left(-k_b^2 w_t\right) \\ &= -k_b^2 \sum_{m,p} \lambda_{mp}^{-1}[\alpha_{mp,t}\mathcal{M}_{\mathcal{S},t}\psi_{mp}(\boldsymbol{r}) + \beta_{mp,t}\mathcal{M}_{\mathcal{S},t}\varphi_{mp}(\boldsymbol{r})]. \end{aligned} \tag{16}$$

The incident field at $\boldsymbol{r}$ is now assumed to be that of a line source located at $\boldsymbol{r}_t$ and can therefore be written as

$$E_t^{\text{inc}}(\boldsymbol{r}) = E^{\text{inc}}(\boldsymbol{r}; \boldsymbol{r}_t) = \mathcal{H}_b^{-1}\left[-\frac{1}{\rho}\delta(\rho - \rho_t)\delta(\theta - \theta_t)\right] \tag{17}$$

where δ represents the Dirac delta function. Using an eigenfunction expansion for the Dirac delta function, the incident field may be written as an eigenfunction expansion with known coefficients:

$$E_t^{\text{inc}}(\boldsymbol{r}) = -\sum_{m,p} \lambda_{mp}^{-1}[\psi_{mp}(\boldsymbol{r})\psi_{mp}(\boldsymbol{r}_t) + \varphi_{mp}(\boldsymbol{r})\varphi_{mp}(\boldsymbol{r}_t)]. \tag{18}$$

It should be noted that (18) is not a convergent series when $\boldsymbol{r} = \boldsymbol{r}_t$ [23], which reflects the singularity at the source point.

In the above analysis, we have implicitly assumed that $\lambda_{mp} \neq 0$. This assumption is always valid when the background medium is lossy. However, λ_{mp} may become zero for lossless backgrounds. This case has been discussed in [9] and a procedure to treat this problem has been proposed.

4.1. Discretizing the CSI functional using the eigenfunction expansions

We now introduce truncated eigenfunction expansions for the contrast, contrast sources and incident fields into the CSI functional by assuming $m = 0, \ldots, M-1$ and $p = 1, \ldots, P$ for each of the expansions. The measured data corresponding to the tth transmitter are denoted as the vector $f_t \in \mathbb{C}^R$, where R is the number of receivers, chosen to be constant for each transmitter. The unknown vector $a_t \in \mathbb{C}^{2MP}$ contains the coefficients $\alpha_{mp,t}$ and $\beta_{mp,t}$ and the unknown vector $b \in \mathbb{C}^{2MP}$ contains γ_{mp} and μ_{mp}. In order to evaluate the norms involved in the Maxwell regularizer term $\mathcal{C}_{\mathcal{D},n}$ we choose to discretize the domain $\mathcal{D}$ in a uniform rectangular grid. The number of discretized points within $\mathcal{D}$ is denoted by Q. With this notation, matrices $\boldsymbol{Z}_t \in \mathbb{C}^{R\times 2MP}$ and $\boldsymbol{F} \in \mathbb{C}^{Q\times 2MP}$ are introduced in such a way that $\boldsymbol{Z}_t a_t$ and $\boldsymbol{F} a_t$ represent the discrete representation of $\mathcal{M}_{\mathcal{S},t}\mathcal{H}_b^{-1}\left(-k_b^2 w_t\right)$, (16), and $\mathcal{H}_b^{-1}\left(-k_b^2 w_t\right)$, (15), respectively.

We also consider the matrix $\boldsymbol{B} \in \mathbb{R}^{Q\times 2MP}$ such that $\boldsymbol{B}b$ represents the discrete form of the contrast χ, given in (13). The vector $u_t^{\text{inc}} \in \mathbb{C}^Q$ includes the incident field corresponding to the tth transmitter, E_t^{inc}, at the Q discrete points inside $\mathcal{D}$. To avoid the singularity of the incident field at the transmitting antenna location, the Q discretization points are chosen so as to not be collocated with the transmitter locations.

Using these discretized operators and vectors, the cost-functional $\mathcal{C}_n(\chi, w_t)$, (8), can be rewritten as

$$\begin{aligned}\mathcal{F}_n(b, a_t) &= \mathcal{F}_{\mathcal{S}}(a_t) + \mathcal{F}_{\mathcal{D},n}(b, a_t)\\ &= \eta_{\mathcal{S}} \sum_t \| f_t - \boldsymbol{Z}_t a_t \|^2 + \eta_{\mathcal{D},n} \sum_t \left\| u_t^{\text{inc}} \odot (\boldsymbol{B}b) - \boldsymbol{B}a_t + (\boldsymbol{B}b) \odot (\boldsymbol{F}a_t) \right\|^2. \end{aligned} \tag{19}$$

The weights $\eta_{\mathcal{S}}$ and $\eta_{\mathcal{D},n}$ are given by

$$\eta_{\mathcal{S}} = \left(\sum_t \| f_t \|^2 \right)^{-1}, \tag{20}$$

and

$$\eta_{\mathcal{D},n} = \left(\sum_t \left\| u_t^{\text{inc}} \odot (\boldsymbol{B}b_{n-1}) \right\|^2 \right)^{-1}, \tag{21}$$

where $\odot$ denotes the Hadamard, i.e. elementwise, product of two vectors of the same size. The cost-functional $\mathcal{F}_n(b, a_t)$ is then minimized iteratively over b and a_t. Each iteration of the inversion algorithm consists of two parts: (*i*) updating a_t by minimizing $\mathcal{F}_n(b, a_t)$ assuming $b = b_{n-1}$, and (*ii*) updating b by minimizing $\mathcal{F}_n(b, a_t)$ assuming $a_t = a_{t,n}$.

It should be noted that choosing the number of eigenfunctions in the expansion, $M \times P$, can be considered a form of projection-based regularization [24] where the unknown functions are projected into the subspace spanned by the chosen eigenfunctions. But, as compared to projection-based regularization methods which have been utilized in the framework of the Gauss–Newton inversion method, e.g. truncated singular value decomposition (TSVD) and Krylov subspace regularization methods (see [24] and references therein), the stability of the eigenfunction CSI method is not very sensitive to the choice of M and P which defines the subspace dimension. This is probably due to the presence of the Maxwell regularizer in the CSI functional which provides another level of regularization. In fact, the overall regularization associated with the eigenfunction CSI method can be considered as a hybrid regularization [25, 26] where a Tikhonov-based regularization (i.e. the Maxwell regularizer) and a projection-based regularization (i.e. truncating the number of eigenfunctions) are utilized together.

4.2. Updating a_t

Assuming that a_t and b at the $(n-1)$th iteration of the algorithm, i.e. $a_{t,n-1}$ and b_{n-1}, are known, we update a_t as

$$a_{t,n} = a_{t,n-1} + \varsigma_n v_{t,n} \tag{22}$$

where $\varsigma_n \in \mathbb{R}$ is the step size. The empirically modified Polak–Ribière CG direction $v_{t,n}$ is given by [27]

$$v_{t,n} = \begin{cases} 0 & n = 0 \\ g_{t,n} + \dfrac{\mathrm{Re}\{\sum_t g_{t,n}^H (g_{t,n} - g_{t,n-1})\}}{\sum_t g_{t,n-1}^H g_{t,n-1}} v_{t,n-1} & \text{otherwise} \end{cases} \tag{23}$$

where $g_{t,n}$ is the direction of the maximum rate of change in $\mathcal{F}_n(b, a_t)$ with respect to a_t evaluated at $a_{t,n-1}$ and the superscript H denotes the Hermitian operator. The cost-functional $\mathcal{F}_n(b_{n-1}, a_t)$ is a nonlinear real-valued function of complex-valued vectors a_t. Therefore, this functional can be differentiated with respect to a_t and its complex conjugate $\overline{a}_t$, treated as two independent vectors [28–30]. As shown in [30], it is the gradient with respect to $\overline{a}_t$ which determines the direction of the maximum rate of change of $\mathcal{F}_n(b, a_t)$. Therefore,

$$g_{t,n} = \left.\frac{\partial \mathcal{F}_{\mathcal{S}}(a_t)}{\partial \overline{a}_t}\right|_{a_{t,n-1}} + \left.\frac{\partial \mathcal{F}_{\mathcal{D},n}(b, a_t)}{\partial \overline{a}_t}\right|_{b_{n-1}, a_{t,n-1}}. \tag{24}$$

The derivative $\partial \mathcal{F}_{\mathcal{S}}(a_t)/\partial \overline{a}_t|_{a_{t,n-1}}$ is given by

$$\left.\frac{\partial \mathcal{F}_{\mathcal{S}}(a_t)}{\partial \overline{a}_t}\right|_{a_{t,n-1}} = -\eta_{\mathcal{S}} \boldsymbol{Z}_t^H (f_t - \boldsymbol{Z}_t a_{t,n-1}). \tag{25}$$

The derivative $\partial \mathcal{F}_{\mathcal{D}}(b, a_t)/\partial \overline{a}_t|_{b_{n-1}, a_{t,n-1}}$ can be written as

$$\left.\frac{\partial \mathcal{F}_{\mathcal{D},n}(b, a_t)}{\partial \overline{a}_t}\right|_{b_{n-1}, a_{t,n-1}} = -\eta_{\mathcal{D},n} \boldsymbol{B}^H d_{t,n-1} + \eta_{\mathcal{D},n} \boldsymbol{F}^H (\overline{\boldsymbol{B} b_{n-1}} \odot d_{t,n-1}) \tag{26}$$

where

$$d_{t,n-1} = u_t^{\mathrm{inc}} \odot (\boldsymbol{B} b_{n-1}) - \boldsymbol{B} a_{t,n-1} + (\boldsymbol{B} b_{n-1}) \odot (\boldsymbol{F} a_{t,n-1}). \tag{27}$$

The step-length ς_n is found by the minimization

$$\varsigma_n = \arg\min_{\varsigma} \{\mathcal{F}_{\mathcal{S}}(a_{t,n-1} + \varsigma v_{t,n-1}) + \mathcal{F}_{\mathcal{D},n}(b_{n-1}, a_{t,n-1} + \varsigma v_{t,n-1})\} \tag{28}$$

which results in

$$\varsigma_n = -\frac{\mathrm{Re}\left\{\sum_t g_{t,n}^H v_{t,n}\right\}}{\eta_{\mathcal{S}} \sum_t \|\boldsymbol{Z}_t v_{t,n}\|^2 + \eta_{\mathcal{D},n} \sum_t \|-\boldsymbol{B} v_{t,n} + (\boldsymbol{B} b_{n-1}) \odot (\boldsymbol{F} v_{t,n})\|^2}. \tag{29}$$

4.3. Updating b

Assuming that $a_{t,n}$ is known, we minimize $\mathcal{F}_n(b, a_t)$ with respect to b. Noting that $\mathcal{F}_{\mathcal{S}}(a_t)$ does not depend on b, the vector b at the nth iteration of the CSI algorithm may be found as

$$\begin{aligned} \boldsymbol{B} b_n &= \arg\min_{\boldsymbol{B}b} \mathcal{F}_{\mathcal{D},n}(b, a_{t,n}) \\ &= \arg\min_{\boldsymbol{B}b} \eta_{\mathcal{D},n} \left\{ \left\| (\boldsymbol{B} b) \odot \left(u_t^{\mathrm{inc}} + \boldsymbol{F} a_{t,n}\right) - \boldsymbol{B} a_{t,n} \right\|^2 \right\}. \end{aligned} \tag{30}$$

The vector $\boldsymbol{B} b_n$ can then be obtained as

$$\boldsymbol{B} b_n = \left[\sum_t \overline{u}_{t,n} \odot (\boldsymbol{B} a_{t,n})\right] \oslash \left[\sum_t \overline{u}_{t,n} \odot u_{t,n}\right] \tag{31}$$

where $u_{t,n} = u_t^{\mathrm{inc}} + \boldsymbol{F} a_{t,n}$ and $\oslash$ represents the elementwise division (Hadamard division) between two vectors of the same size. It should be noted that finding b_n from $\boldsymbol{B} b_n$ is not necessary as updating a_t requires $\boldsymbol{B} b$, not b.

4.4. Initial guess for a_t

The CSI algorithm requires an initial guess for a_t and b at the beginning of the algorithm. One method might be to assume a zero initial guess for a_t as well as b and then update a_t using the steepest descent algorithm (which is traditionally the first step of any conjugate gradient algorithm). If this route is followed then a choice would need to be made on the normalization term $\eta_{\mathcal{D},n}$ which is undefined at the first step for this choice of initial guess. One approach might be to use prior information on the value of the contrast to provide a non-zero $\boldsymbol{B}b$. Alternatively, one could ignore the Maxwell regularizer, by assuming $\eta_{\mathcal{D},n} = 0$, and minimize the data-error functional, $\mathcal{F}_{\mathcal{S}}(a_t)$, on its own, using perhaps, a single step in the steepest descent direction.

The method that we choose allows some flexibility in that this data-error functional minimization is approached using Krylov subspace regularization. Explicitly, the initial guess for a_t may be found by

$$a_{t,0} = \arg\min_{a_t}\{\| f_t - \boldsymbol{Z} a_t \|^2\} \tag{32}$$

subject to a Krylov subspace regularization technique, e.g. the conjugate gradient least squares (CGLS) method [31]. These iterative algorithms, when applied to an ill-posed system of equations like (32), exhibit a *semi-convergence* behavior [26]. That is, they improve the solution at their early iterations, where the solution space is restricted to a Krylov subspace of small dimension. However, they start deteriorating the solution by inverting the noise—in our case, the noise in f_t—in later iterations. An appropriately regularized solution can therefore be obtained by early termination of the utilized Krylov subspace algorithm when the dimension of the subspace is large enough to produce a good regularized solution and small enough to suppress the effect of noise. Therefore, the iteration at which the algorithm is stopped plays the role of the regularization parameter for this type of regularization: the fewer the iterations, the stronger the regularization.

To find $a_{t,0}$, we utilize the CGLS algorithm as the Krylov subspace regularization and choose the maximum possible regularization weight of this regularization. That is, only one iteration of the CGLS algorithm is applied to the least squares problem $\boldsymbol{Z}_t a_t = f_t$. The initial guess to the CGLS method is considered to be the zero vector of appropriate size. Therefore, the regularized solution $a_{t,0}$ will be $a_{t,0} = \xi_t h_t$ where h_t is the CG direction at the first iteration of the CGLS algorithm (that is, the steepest descent direction) applied to $\boldsymbol{Z}_t a_t = f_t$ and ξ_t is the CGLS step size. Finding h_t and ξ_t, the regularized solution $a_{t,0}$ can be written as

$$a_{t,0} = \frac{\left\| \boldsymbol{Z}_t^H f_t \right\|^2}{\left\| \boldsymbol{Z}_t \boldsymbol{Z}_t^H f_t \right\|^2} \boldsymbol{Z}_t^H f_t. \tag{33}$$

We note that (33) is equivalent to the backpropagation solution, given in [2, 18]. The formulation as a Krylov subspace regularized minimization of the data-error functional gives us the option of performing more than the first steepest descent step. Unfortunately, finding the optimum stopping iteration in these methods is difficult and, because we rely on the Maxwell regularizer, we have found that there is no need to use more than the first few steps of the Krylov-based method to obtain the initial value of a_t. In fact, in all the results presented herein, only the first step is used, because no advantage was gained in using more than the first step. Having found $a_{t,0}$, the vector $\boldsymbol{B}b_0$ can be found from (31).

5. Inversion results

In this section, we show inversion results for three synthetic data sets and one preliminary experimental data set. All synthetic data sets have been created with a frequency-domain finite element method (FEM) forward solver. To all synthetic data sets, 3% noise was added using the formula [32]

$$f_t = f_t^{\text{FEM}} + \max\left[\forall_t \; f_t^{\text{FEM}}\right] \frac{\eta}{\sqrt{2}}(\tau_1 + j\tau_2) \tag{34}$$

where f_t^{FEM} is the scattered field on the measurement domain obtained by the FEM forward solver, τ_1 and τ_2 are two real vectors whose elements are uniformly distributed zero-mean random numbers between -1 and 1, and $\eta = 0.03$. The noisy data f_t are then used to test the inversion algorithm against three synthetic data sets. To show the robustness of the inversion algorithm with respect to the noise level η, we also show inversion results of the third data set when η is chosen to be 0.15 and 0.25.

We avoid frequencies associated with the zero eigenvalue since at such frequencies the inverse operator $\mathcal{H}_b^{-1}$ does not exist. That is, no resonant frequencies have been chosen. In addition, all examples are run with no prior information and the only constraint imposed on the contrast is that the corresponding relative permittivity should be physical (i.e. the real part of the relative permittivity is kept greater than 1, and the imaginary part is kept non-negative). In all inversions considered herein, unless otherwise stated, we assume $M = P = 30$. Utilizing $M = P = 30$, i.e. projecting the unknown contrast into 900 eigenfunctions, provides stable solutions for the data sets considered herein. Increasing the number of eigenfunctions to $M = P = 40$ and $M = P = 50$ results in very similar reconstructions compared to the results obtained using $M = P = 30$. However, the inversion results start to deteriorate when M and P are chosen to be more than 50. For the first data set, we show the performance of the eigenfunction CSI method using five different sets of values for M and P.

In all synthetic data sets considered herein, we show the *direct* eigenfunction expansion for the exact dielectric profile of the OI (for $M = P = 30$) which is obtained from expansion (13) with coefficients computed by taking the inner product of the exact contrast with the expansion. We call this direct expansion the theoretical limit for the method given the chosen number of eigenfunction terms. We also define the error between the direct expansion and the reconstructed expansion as

$$EE = \frac{\left\| \epsilon_{MP} - \epsilon_{MP}^d \right\|}{\left\| \epsilon_{MP}^d \right\|} \tag{35}$$

where ϵ_{MP} and ϵ_{MP}^d are the reconstructed and direct eigenfunction expansions of the relative permittivity respectively. This *eigenfunction error*, EE, is most easily computed using Parseval's theorem.

For the targets considered in the the three synthetic data sets, we also show the inversion results from the scattering data collected in an open-region background using the integral equation-based CSI method [18]. We refer to this algorithm as the IE-CSI method. In all of these open-region reconstructions, we have used the same transmitters and receivers as used in the eigenfunction CSI method. We have also used $\eta = 0.03$ to generate noisy scattering data for the open-region cases. For the conductive enclosure experimental data set, we also show the inversion results using the Gauss–Newton inversion method [11].

5.1. Synthetic data set I: concentric squares

For the first numerical example, we consider the OI to be two concentric squares. This target has been used in other publications such as [10, 18, 33, 34]. The inner square has a dimension

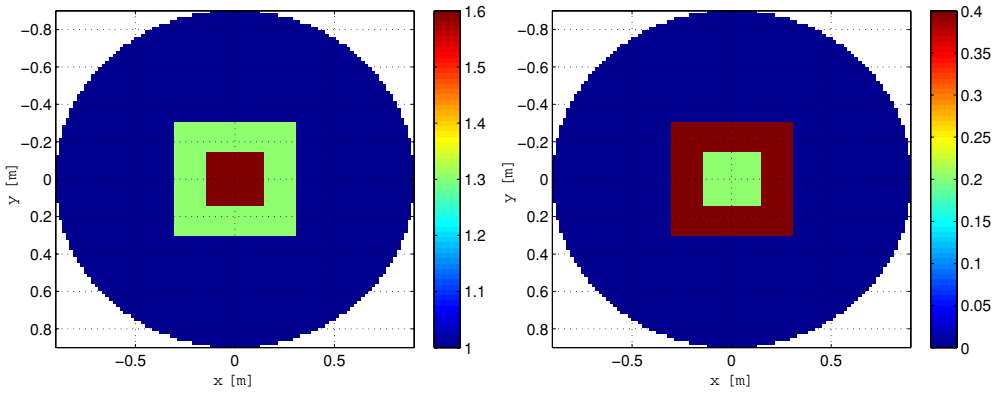

(a) Exact $Re(\epsilon)$ (b) Exact $Im(\epsilon)$

Figure 2. Exact relative permittivity for the concentric squares data set.

of $\lambda_b \times \lambda_b$ (λ_b is the wavelength in the background medium) with a relative permittivity of $1.6 + j0.2$. The inner square is surrounded by an exterior square having sides of $2\lambda_b$ and relative permittivity of $1.3 + j0.4$. The OI is surrounded by a circular PEC cylinder of radius $3\lambda_b$. The exact permittivity profile is shown in figure 2. The frequency of operation is chosen to be 1 GHz and the relative permittivity of the background medium is assumed to be $\epsilon_b = 1$; thus, $\lambda_b = 0.3$ m. The OI is illuminated by 30 transmitters evenly spaced on a circle of radius $2.33\lambda_b$. The data are then collected using 40 transmitters evenly spaced on a circle of radius $2.17\lambda_b$.

The inversion algorithm is tested against this data set in five different cases distinguished by the number of eigenfunctions used: (*i*) 100 ($M = P = 10$), (*ii*) 400 ($M = P = 20$), (*iii*) 900 ($M = P = 30$), (*iv*) 2500 ($M = P = 50$) and (*v*) 4900 ($M = P = 70$). The inversion result for the first case is shown in figures 3(a), (b) where it can be seen that the two concentric squares are not resolved. Increasing the number of eigenfunctions in the second case to 400, the algorithm does a good job of resolving the two squares and reconstructs their complex relative permittivities as shown in figures 3(c), (d). In the third case, shown in figures 3(e), (f), the edges of the squares are sharper compared to the second case. The direct eigenfunction expansion for the exact dielectric profile of the OI (for $M = P = 30$) is shown in figures 3(g), (h) where the corresponding EE is 0.03. Increasing the number of eigenfunctions in the fourth case to 2500, the reconstruction result, see figures 4(a), (b), remained similar to the $M = P = 30$ case. However, the inversion results start to deteriorate when M and P are chosen to be more than 50. In figures 4(c), (d), we have shown the inversion result for the fifth case ($M = P = 70$) where the inversion algorithm cannot produce an acceptable reconstruction for the OI. The computational time of the eigenfunction CSI method for the $M = P = 30$ case was 1.36 s per CSI iteration (23 min in total) on a 2.66 GHz machine. The open-region reconstruction of this target using the IE-CSI method is shown in figure 5.

5.2. Synthetic data set II: resolution test

For this data set, the OI consists of two circular cylinders of radius 0.02 m with a relative permittivity of $\epsilon = 2$. The OI is located in a background medium with relative permittivity $\epsilon = 1$ and enclosed by a circular PEC enclosure of radius 0.12 m. The OI is illuminated by 16 transmitters at the frequency of $f = 1.2$ GHz and the data are collected using 16 receivers per

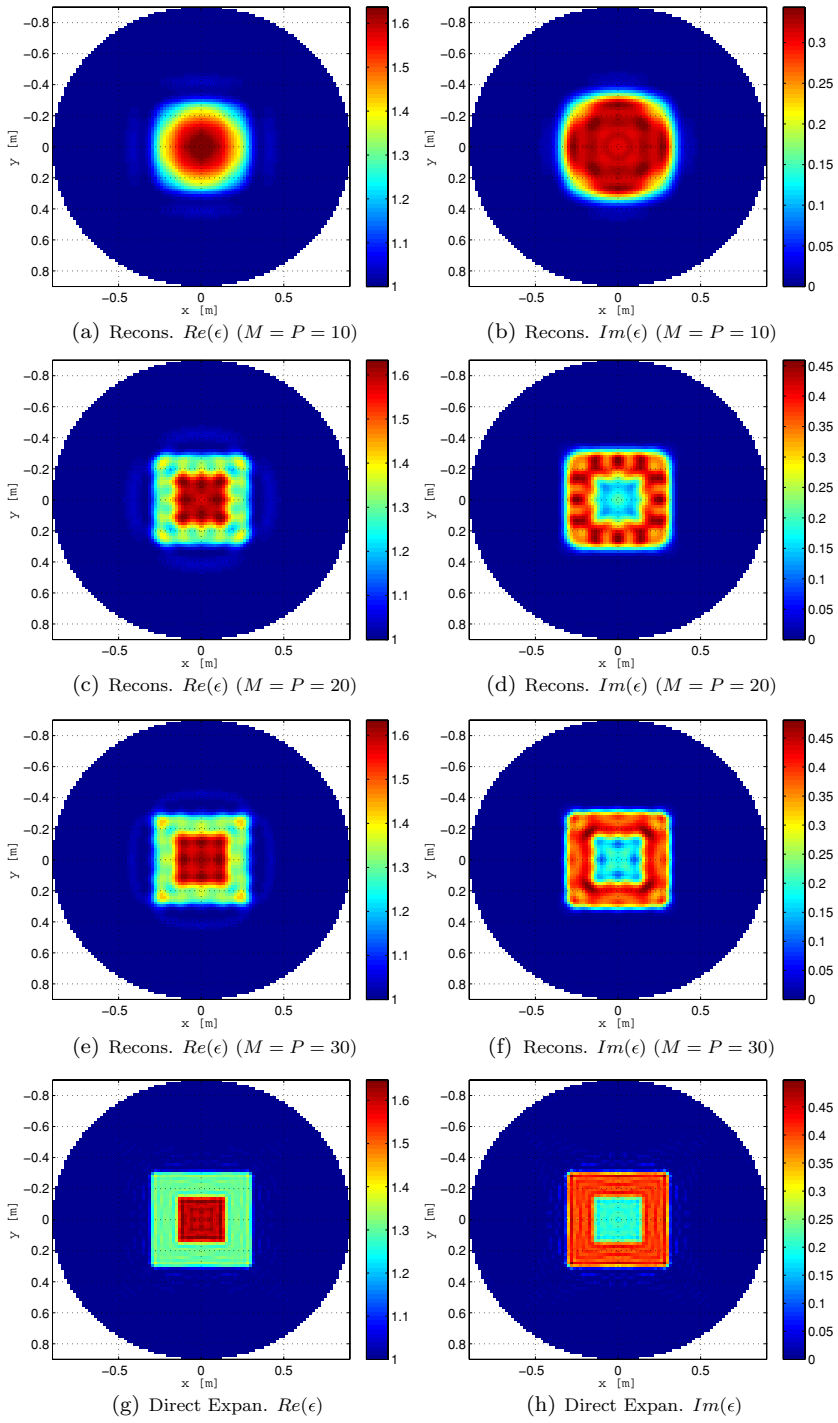

(a) Recons. $Re(\epsilon)$ $(M = P = 10)$ (b) Recons. $Im(\epsilon)$ $(M = P = 10)$

(c) Recons. $Re(\epsilon)$ $(M = P = 20)$ (d) Recons. $Im(\epsilon)$ $(M = P = 20)$

(e) Recons. $Re(\epsilon)$ $(M = P = 30)$ (f) Recons. $Im(\epsilon)$ $(M = P = 30)$

(g) Direct Expan. $Re(\epsilon)$ (h) Direct Expan. $Im(\epsilon)$

Figure 3. Concentric squares data set (a), (b) eigenfunction CSI reconstruction when $M = P = 10$, (c), (d) eigenfunction CSI reconstruction when $M = P = 20$, (e), (f) eigenfunction CSI reconstruction when $M = P = 30$, and (g), (h) direct eigenfunction expansion of the exact dielectric profile of the object of interest ($M = P = 30$).

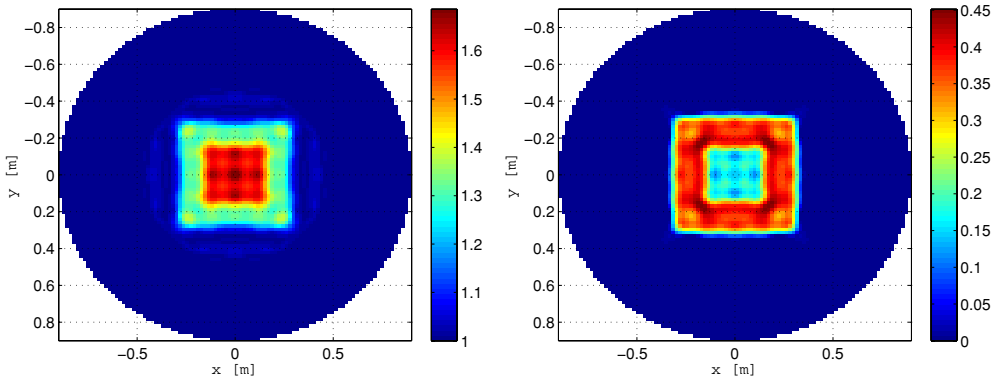

(a) Recons. $Re(\epsilon)$ $(M = P = 50)$ (b) Recons. $Im(\epsilon)$ $(M = P = 50)$

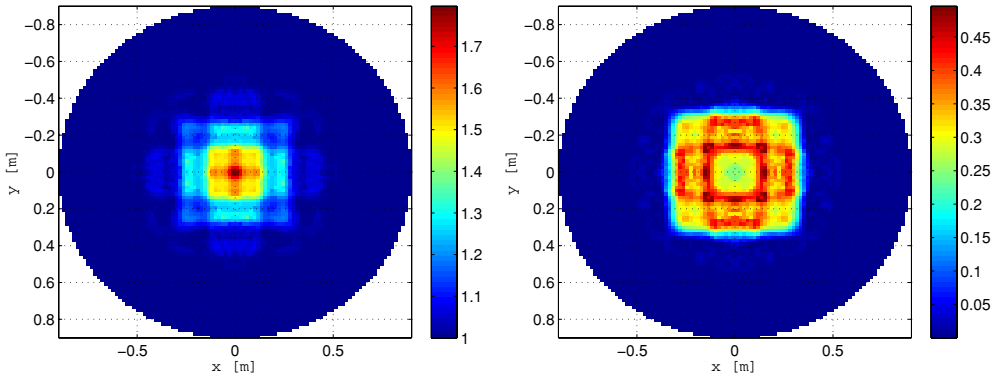

(c) Recons. $Re(\epsilon)$ $(M = P = 70)$ (d) Recons. $Im(\epsilon)$ $(M = P = 70)$

Figure 4. Concentric squares data set: (a), (b) eigenfunction CSI reconstruction when $M = P = 50$, and (c), (d) eigenfunction CSI reconstruction when $M = P = 70$.

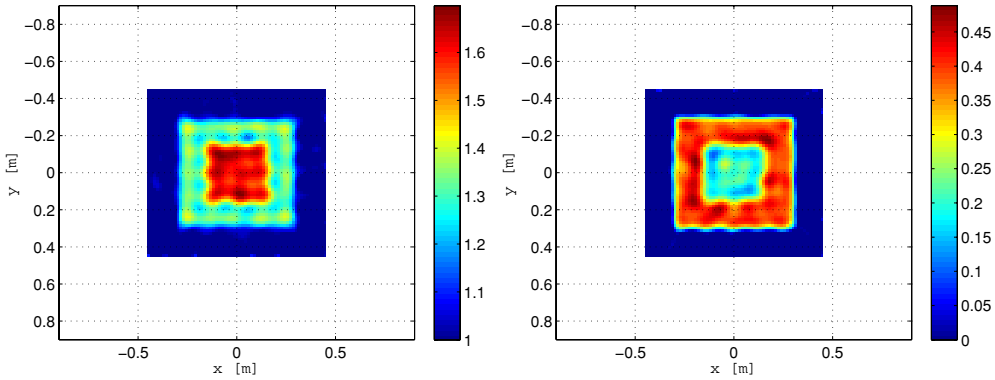

(a) Recons. $Re(\epsilon)$ (b) Recons. $Im(\epsilon)$

Figure 5. Concentric squares data set: open-region IE-CSI reconstruction. The imaging domain is a 0.9 m × 0.9 m square.

transmitter. Transmitting and receiving antennas are evenly spaced on a circle of radius 0.1 m. We consider three different scenarios which are distinguished by the distance between the centers of the two circular targets. The three choices for this distance are (*i*) $0.4\lambda_b = 0.1$ m,

(*ii*) $0.32\lambda_b = 0.08$ m and (*iii*) $0.24\lambda_b = 0.06$ m. Note that the diameter of each cylinder is only $0.16\lambda_b$.

In the first scenario, where the exact relative permittivity profile is shown in figures 6(a), (b), the inversion algorithm is able to resolve these two scatterers and reconstruct their permittivities. The reconstructed permittivity in this case is shown in figures 6(c), (d) which has a very small imaginary part, showing that the targets are lossless. The direct eigenfunction expansion for the exact dielectric profile of the OI (for $M = P = 30$) is shown in figures 6(e), (f) where the corresponding EE is 0.07. The open-region reconstruction of this target using the IE-CSI method is shown in figures 6(g), (h). Reducing the distance of the two targets' centers to $0.32\lambda_b$ in the second scenario, figures 7(a), (b), the inversion algorithm is still able to reconstruct the scatterers which is shown in figures 7(c), (d). The direct eigenfunction expansion of the true dielectric profile is shown in figures 7(e), (f). The corresponding EE is 0.08 for this case. The open-region reconstruction for this target is shown in figures 7(g), (h). In the third scenario, shown in figures 8(a), (b), the inversion algorithm is not able to resolve the two scatterers (see figures 8(c), (d)). The direct eigenfunction expansion of the true dielectric profile for this case is shown in figures 8(e), (f) where the corresponding $EE = 0.10$. The open-region reconstruction for this target is shown in figures 8(g), (h). The computational time of the eigenfunction CSI method for each of these scenarios was about 1.25 s per CSI iteration (21 min in total) on a 2.66 GHz machine.

5.3. Synthetic data set III: circular targets with lossy background

We consider an OI which consists of three circular regions. Two of these circular regions have the same radius of 0.015 m and their relative complex permittivities are $40 + j10$ and $30 + j15$. These two circular regions are surrounded by another circular region with radius of 0.06 m and relative permittivity of 12. The OI is immersed in a lossy background and enclosed by a circular PEC enclosure of radius 0.12 m. The object of interest is successively irradiated by 32 transmitters evenly spaced on a circle of radius 0.1 m. The data are collected using 32 receivers per transmitter where the receiver locations are the same as the transmitter locations. The frequency of operation is chosen to be 1 GHz at which the complex permittivity of the background medium is $23.4 + j1.13$. The OI is shown in figures 9(a), (b) and the reconstructed permittivity using the eigenfunction contrast source inversion method is shown in figures 9(c), (d). The direct eigenfunction expansion for the exact dielectric profile of the OI (for $M = P = 30$) is shown in figures 9(e), (f) where the corresponding EE is 0.11. The computational time for this target was 1.90 s (21 min in total) on a 2.66 GHz machine. The open-region reconstruction for this target is shown in figures 9(g), (h). To show the robustness of the eigenfunction CSI algorithm with respect to the noise level, the inversion results of this target when the noise level is 15% and 25% are shown in figures 10(a), (b) and figures 10(c), (d) respectively.

5.4. Experimental data set

We also present preliminary results from the University of Manitoba MWI system with circular metallic casing which is currently under development, see figure 11(a). We have employed a two-port Agilent 8363B PNA-Series Network Analyzer (NA) as our microwave source and receiver. The NA is connected to the antennas with a 2×24 crossbar mechanical switch (Agilent 87050A-K24). Twenty-four monopole antennas are arranged at even intervals of 15° in a circular array at the midpoint height along the inside of a stainless steel cylinder of radius 0.224 m, and height 0.508 m. The monopole antennas, shown in figure 11(b), are simple

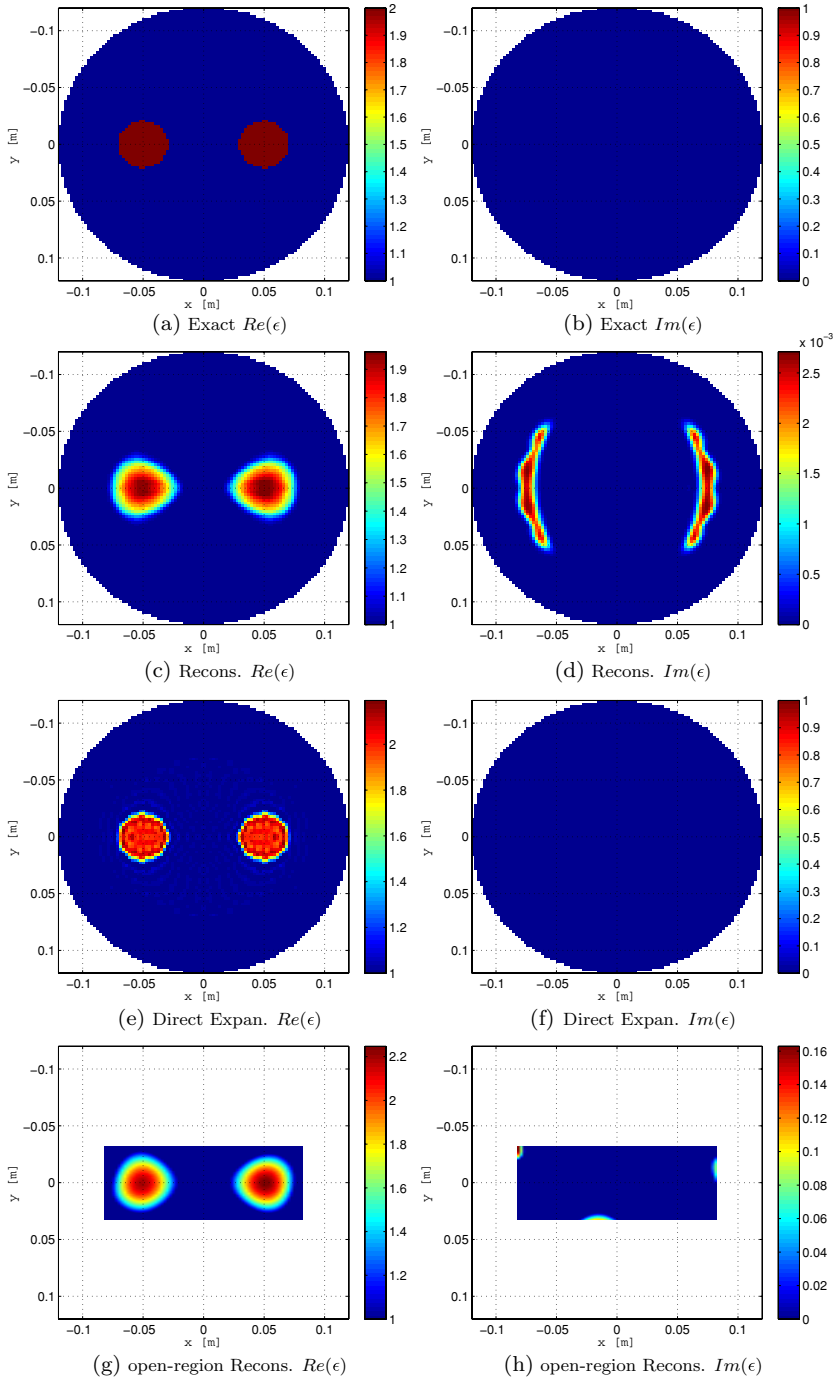

Figure 6. Resolution Test (1st scenario) (a), (b) exact relative permittivity of the object of interest, (c), (d) eigenfunction CSI reconstruction, (e), (f) direct eigenfunction expansion of the exact dielectric profile of the object of interest ($M = P = 30$), and (g), (h) open-region reconstruction of the object of interest using the IE-CSI method. For the eigenfunction CSI method, the imaging domain is the whole interior of the metallic enclosure whereas for the open-region IE-CSI method, it is a 0.164 m $\times$ 0.064 m rectangle.

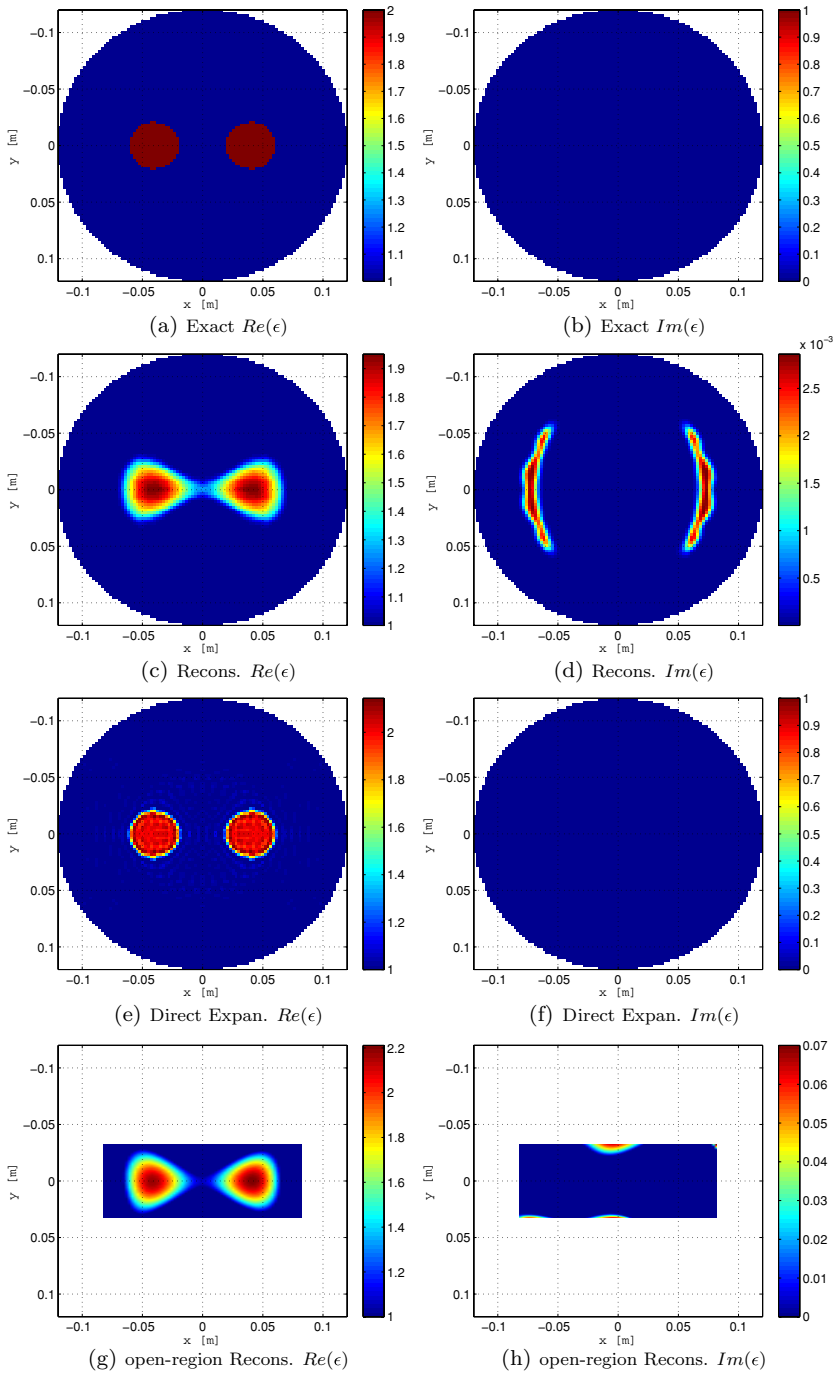

Figure 7. Resolution Test (2nd scenario) (a), (b) exact relative permittivity of the object of interest, (c), (d) eigenfunction CSI reconstruction, (e), (f) direct eigenfunction expansion of the exact dielectric profile of the object of interest ($M = P = 30$), and (g), (h) open-region reconstruction of the object of interest using the IE-CSI method. For the eigenfunction CSI method, the imaging domain is the whole interior of the metallic enclosure whereas for the open-region IE-CSI method, it is a 0.164 m $\times$ 0.064 m rectangle.

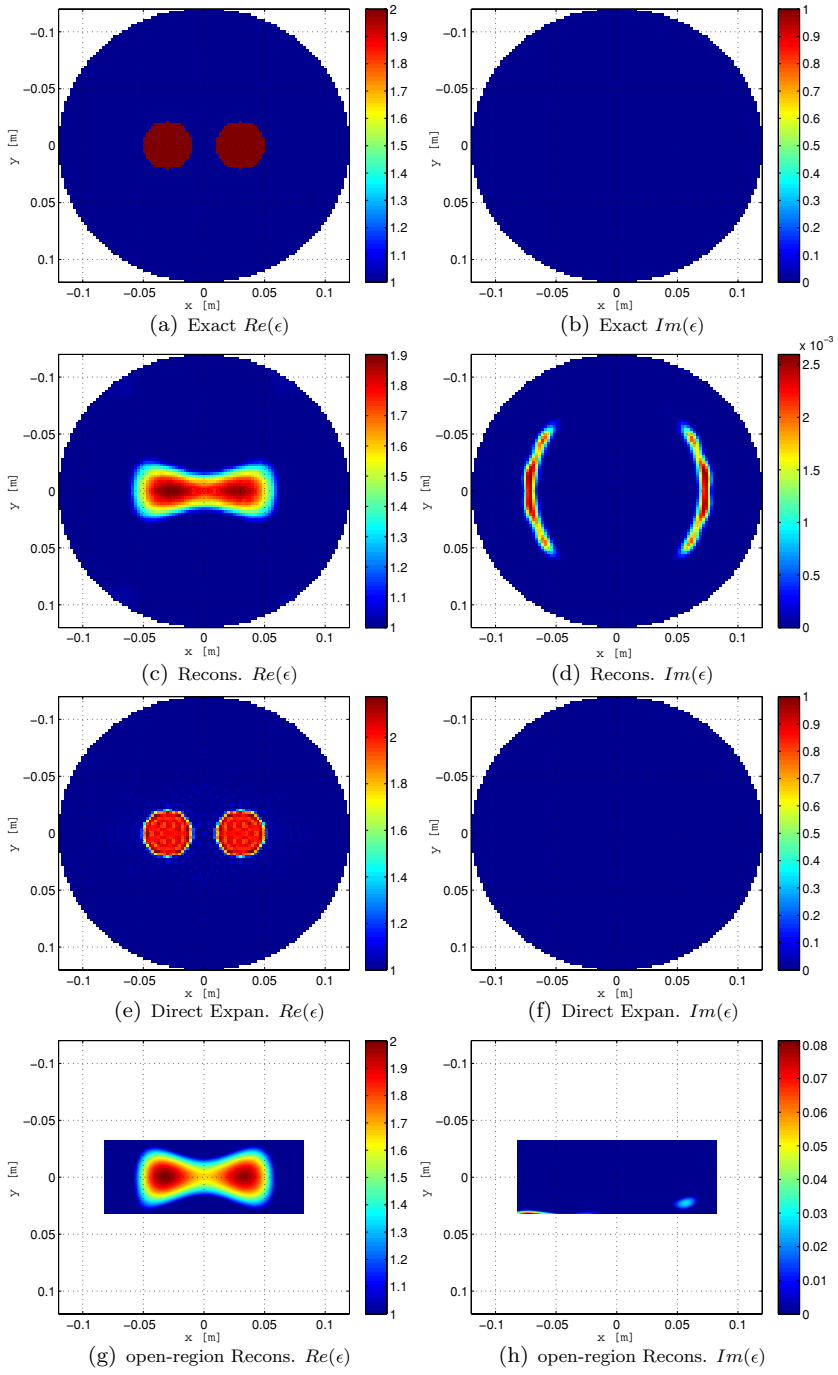

Figure 8. Resolution Test (3rd scenario) (a), (b) exact relative permittivity of the object of interest, (c), (d) eigenfunction CSI reconstruction, (e), (f) direct eigenfunction expansion of the exact dielectric profile of the object of interest ($M = P = 30$), and (g), (h) open-region reconstruction of the object of interest using the IE-CSI method. For the eigenfunction CSI method, the imaging domain is the whole interior of the metallic enclosure whereas for the open-region IE-CSI method, it is a 0.164 m $\times$ 0.064 m rectangle.

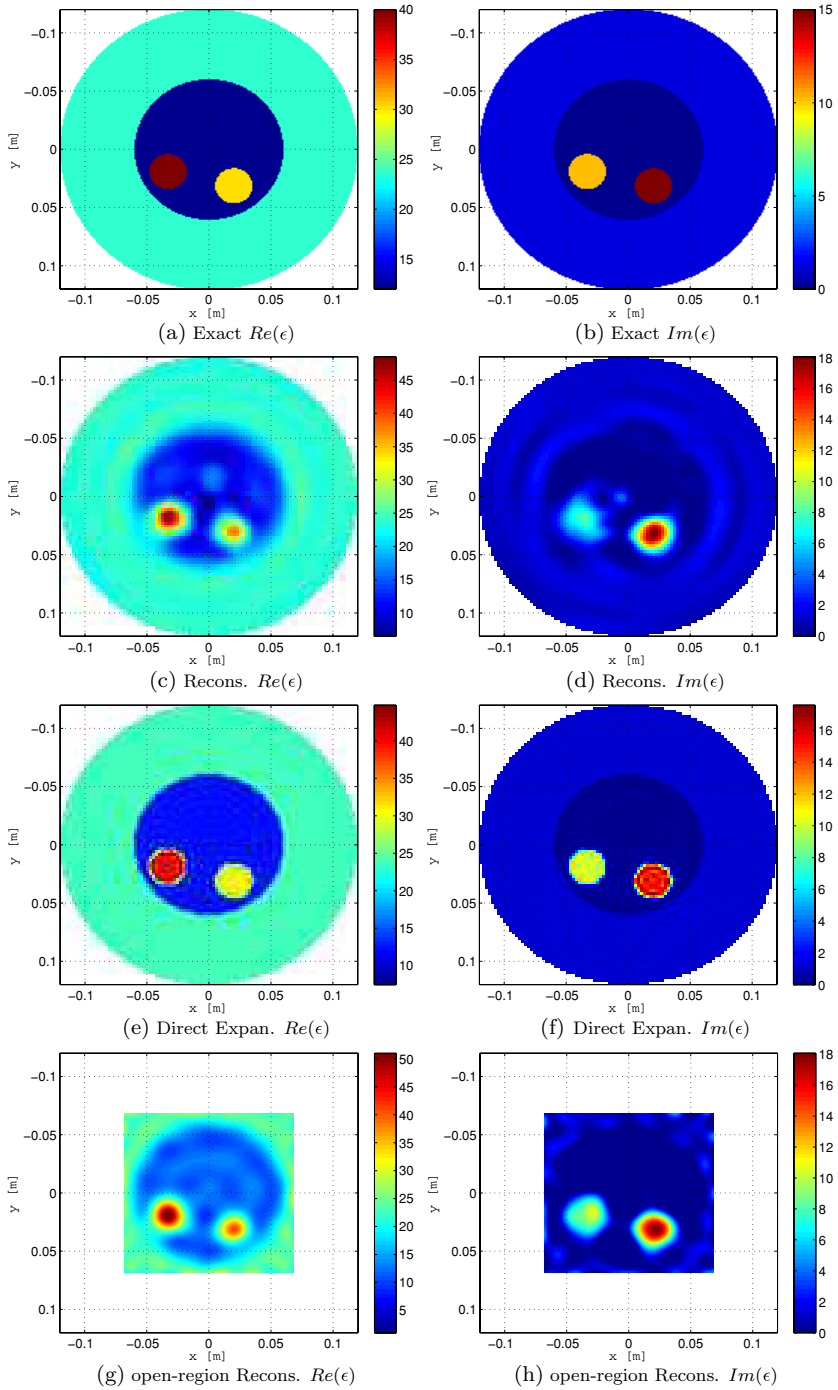

Figure 9. Synthetic data set III (a), (b) exact relative permittivity of the object of interest (c), (d) eigenfunction CSI reconstruction, (e), (f) direct eigenfunction expansion of the exact dielectric profile of the object of interest ($M = P = 30$), and (g), (h) open-region reconstruction of the object of interest using the IE-CSI method. For the eigenfunction CSI method, the imaging domain is the whole interior of the metallic enclosure whereas for the open-region IE-CSI method, it is a 0.136 m $\times$ 0.136 m square.

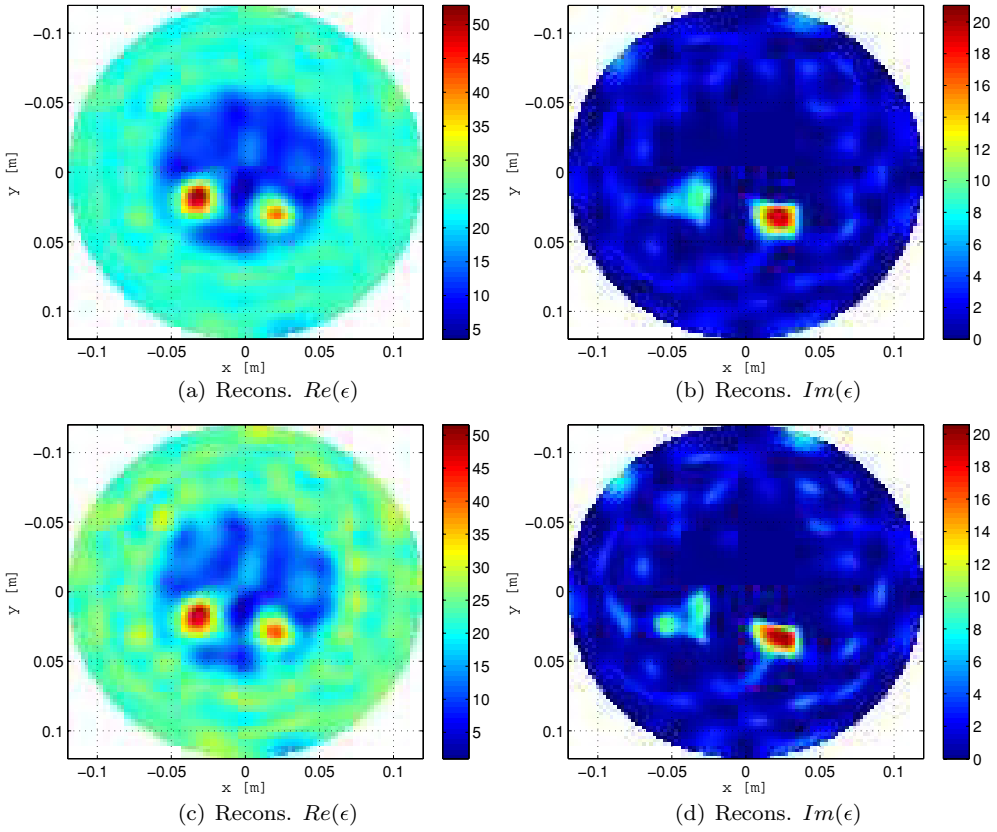

(a) Recons. $Re(\epsilon)$ (b) Recons. $Im(\epsilon)$

(c) Recons. $Re(\epsilon)$ (d) Recons. $Im(\epsilon)$

Figure 10. Eigenfunction CSI reconstruction of the synthetic data set III with (a), (b) 15% noise ($\eta = 0.15$), and (c), (d) 25% noise ($\eta = 0.25$).

wires with right-angle bends placed into the female end of the bulk-head SMA connectors that protrude into the wall of the cylinder. These monopoles are oriented in the vertical direction, parallel to the cylindrical walls. The distance of the antennas from the wall of the chamber is only 0.01 m. Other resistively loaded antennas have been investigated, but the system design is not part of the current study. Although the stainless steel enclosure is water-tight, allowing it to be filled with a matching liquid, the background medium for this data is air. The OI is an approximately square wooden cylinder with side length ≈ 0.09 m and a height of ≈ 0.3 m. Using an Agilent 85070E dielectric probe kit, we measured the wood to have a relative permittivity of $\epsilon \approx 2 + j0.2$ at the 1 GHz frequency which was used. The target was placed at the center of the metallic chamber, shown in figure 11(a), and 23×24 measurements were taken at this frequency (23 receivers per transmitter).

The vector network analyzer collects scattering parameters between antenna ports. Note that the 24 antennas are co-resident during all measurements. As the imaging algorithm requires scattered field measurements, the data are first collected for the MWI system in the absence of the OI. Assuming that the tth transmitter is active, these data are labeled as the *incident* measurement $S^{\text{inc}}_{21,t}$, and consist of 23 measurements. We then perform the same experiment in the presence of the OI. This data set is labeled as the *total* measurement $S_{21,t}$. The measured incident data are then subtracted from the measured total data and are denoted by the measured *scattered* data, $S^{\text{scat}}_{21,t} = S_{21,t} - S^{\text{inc}}_{21,t}$.

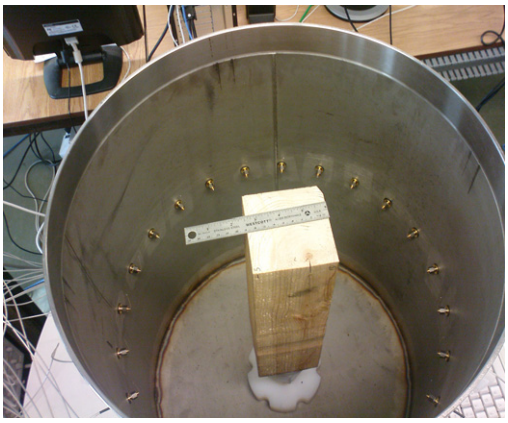

(a) Dielectric phantom target inside the MWI system

(b) Monopole antenna

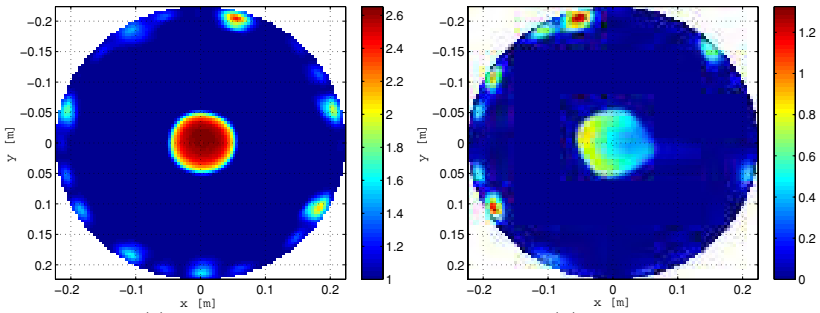

(c) Recons. $Re(\epsilon)$ (d) Recons. $Im(\epsilon)$

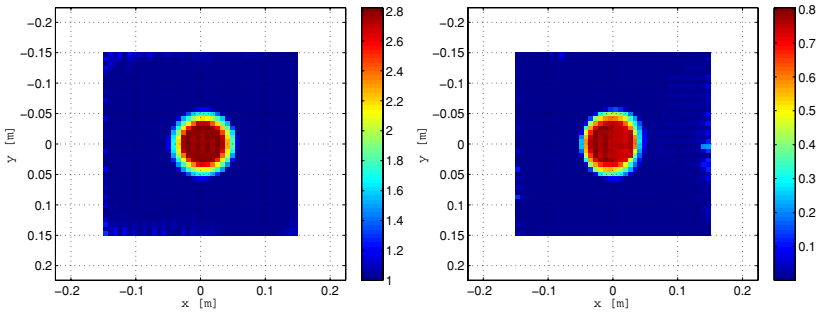

(e) Recons. $Re(\epsilon)$ (f) Recons. $Im(\epsilon)$

Figure 11. Experimental data set (a) the object of interest inside the circular metallic enclosure, (b) monopole antenna, (c), (d) eigenfunction CSI reconstruction, and (e), (f) Gauss-Newton reconstruction. For the eigenfunction CSI method, the imaging domain is the whole interior of the metallic enclosure whereas for the Gauss–Newton inversion, it is a 0.3 m × 0.3 m square.

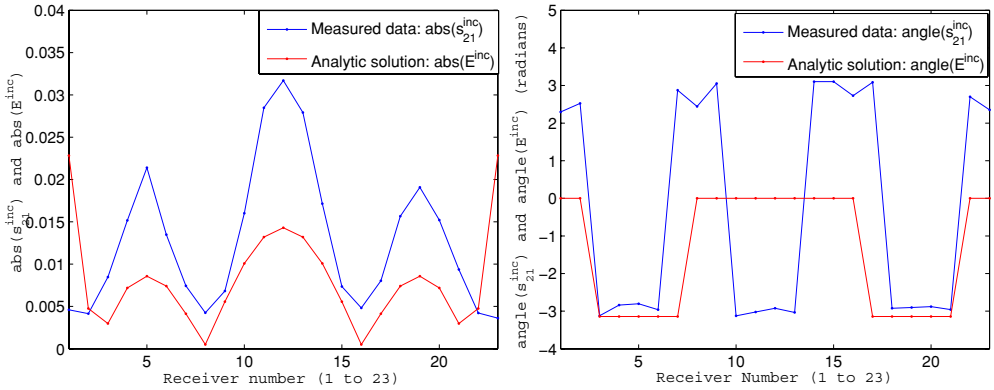

(a) Absolute value (b) Phase value

Figure 12. Comparison of the simulated incident field and the measured S_{21}^{inc} for the first transmitter at the 23 receiver locations (a) absolute value, and (b) phase.

Modeling the incident field inside the target, which cannot be obtained via measurement, by E_t^{inc} given in (18), the calibrated measured scattered fields for the unknown target corresponding to the tth transmitter are calculated by

$$E_t^{\text{meas}}(\boldsymbol{r}) = \frac{E_t^{\text{inc}}(\boldsymbol{r})}{S_{21,t}^{\text{inc}}(\boldsymbol{r})} S_{21,t}^{\text{scat}}(\boldsymbol{r}), \tag{36}$$

where $\boldsymbol{r} \in \mathcal{S}$. The field $E_t^{\text{meas}}(\boldsymbol{r} \in \mathcal{S})$, denoted by f_t in its vectorized form, is then used in the inversion algorithm. The measured $S_{21,t}^{\text{inc}}(\boldsymbol{r})$ and the simulated $E_t^{\text{inc}}(\boldsymbol{r})$ corresponding to the first transmitter, $t = 1$, are shown in figure 12 at the 23 receiver locations. This frequency was chosen because of the reasonable match between the raw S_{21}^{inc} and the analytic incident field assumed in the inversion model. Although this calibration technique is the one that has been successfully used to calibrate the Fresnel 2001 and 2005 data sets [35, 36] (collected in an anechoic chamber), it is not ideally suited to measurements taken inside conductive enclosures because the mutual coupling between the co-resident antennas is much greater than that in open-region systems.

The inversion result using eigenfunction contrast source inversion is shown in figures 11(c), (d). As can be seen, the shape of the square wooden cylinder is not resolved and the reconstructed permittivity is over the measured value. The computational time for this target was 1.30 s (22 min in total) on a 2.66 GHz machine. We also note the artifacts due to the presence of the antennas. To check whether the poor inversion result is due to the use of eigenfunction CSI or the calibrated measured data itself, we have also inverted the calibrated measured data using the state-of-the-art Gauss–Newton Inversion (GNI) algorithm [11]. The inversion results using the GNI method are shown in figures 11(e), (f). As can be seen the reconstruction results from the eigenfunction CSI and the GNI method are very similar. We speculate that the poor performance of these two inversion algorithms against the measured data are due to the high mutual coupling between the 24 co-resident antennas which needs to be either modeled in the inversion algorithm (e.g. see [37]) or calibrated out by an appropriate improved calibration technique. It is expected that by using either of these methods the eigenfunction CSI method, and also the GNI method, would perform much better with the experimental data. The investigation of improved calibration techniques for conductive enclosure MWI systems is the subject of on-going research.

6. Conclusion

In this paper, we have presented a new eigenfunction CSI method. This method is based on expressing the unknown contrast and contrast sources as truncated eigenfunction expansions corresponding to the Helmholtz operator in a homogeneous background medium. The expansion coefficients become the unknowns in the inverse problem which is formulated by introducing these eigenfunction expansions into the CSI functional. The traditional CG technique is used to minimize the functional with respect to these expansion coefficients. No prior information is used other than constraining the resulting permittivity profile to be physical. The inversion algorithm was tested against both synthetically and experimentally collected data. Results for the synthetically generated data are excellent compared to results on the same data that can be generated using state-of-the-art inversion algorithms such as the Gauss–Newton inversion [11, 15]. Preliminary results of inverting experimental data produced poor results, but it is our expectation that there will be much improvement in the experimental reconstructions once better calibration procedures are implemented which is part of future work.

Acknowledgments

We would like to thank Amer Zakaria for providing the FEM forward solver and the experimental data set. We would also like to thank Cameron Kaye for help in collecting some of the experimental data. We also gratefully acknowledge the financial support of the Natural Sciences and Engineering Research Council of Canada.

References

[1] Rubæk T, Meaney P M, Meincke P and Paulsen K D 2007 Nonlinear microwave imaging for breast-cancer screening using Gauss-Newton's method and the CGLS inversion algorithm *IEEE Trans. Antennas Propag.* **55** 2320–31

[2] Abubakar A, van den Berg P M and Mallorqui J J 2002 Imaging of biomedical data using a multiplicative regularized contrast source inversion method *IEEE Trans. Microw. Theory Tech.* **50** 1761–77

[3] Bulyshev A E, Souvorov A E, Semenov S Y, Svenson R H, Nazarov A G, Sizov Y E and Tastis G P 2000 Three dimensional microwave tomography: theory and computer experiments in scalar approximation *Inverse Probl.* **16** 863–75

[4] Semenov S Y *et al* 2002 Three-dimensional microwave tomography: initial experimental imaging of animals *IEEE Trans. Biomed. Eng.* **49** 55–63

[5] Meaney P M, Fanning M W, Li E, Poplack S P and Paulsen K D 2000 A clinical prototype for active microwave imaging of the breast *IEEE Trans. Microw. Theory Tech.* **48** 1841–53

[6] Yu C, Yuan M, Stang J, Bresslour E, George R T, Ybarra G A, Joines W T and Liu Q H 2008 Active microwave imaging II: 3-D system prototype and image reconstruction from experimental data *IEEE Trans. Microw. Theory Tech.* **56** 991–1000

[7] Fhager A, Hashemzadeh P and Persson M 2006 Reconstruction quality and spectral content of an electromagnetic time-domain inversion algorithm *IEEE Trans. Biomed. Eng.* **53** 1594–604

[8] Rubæk T and Zhurbenko V Prototype of microwave imaging system for breast-cancer screening *Proc. 13th Int. Symp. on Antenna Technology and Applied Electromagnetics and the Canadian Radio Science Meeting (ANTEM/URSI)* (Banff, Canada, February 2009)

[9] Crocco L and Litman A 2009 On embedded microwave imaging systems: retrievable information and design guidelines *Inverse Probl.* **25** 065001 (17pp)

[10] Gilmore C and LoVetri J 2008 Enhancement of microwave tomography through the use of electrically conducting enclosures *Inverse Probl.* **24** 035008 (21pp)

[11] Mojabi P, Gilmore C, Zakaria A and LoVetri J 2009 Biomedical microwave inversion in conducting cylinders of arbitrary shapes *13th Int. Symp. on Antenna Technology and Applied Electromagnetics and the Canadian Radio Science Meeting (ANTEM/URSI)* pp 1–4

[12] Semenov S Y, Svenson R H, Bulyshev A E, Souvorov A E, Nazarov A G, Sizov Y E, Posukh V G, Pavlovsky A V, Repin P N and Tatsis G P 2000 Spatial resolution of microwave tomography for detection of myocardial ischemia and infarction-experimental study on two-dimensional models *IEEE Trans. Microw. Theory Tech.* **48** 538–44
[13] Meaney P M, Paulsen K D, Hartov A and Crane R K 1996 Microwave imaging for tissue assessment: initial evaluation in multitarget tissue-equivalent phantoms *IEEE Trans. Biomed. Eng.* **43** 878–90
[14] van den Berg P M and Fokkema J T 2003 Removal of undesired wavefields related to the casing of a microwave scanner *IEEE Trans. Microw. Theory Tech.* **51** 187–92
[15] Franchois A and Tijhuis A G 2003 A quasi-Newton reconstruction algorithm for a complex microwave imaging scanner environment *Radio Sci.* **38**
[16] Lencrerot R, Litman A, Tortel H and Geffrin J-M 2009 Measurement strategies for a confined microwave circular scanner *Inverse Probl. Sci. Eng.* 1–16
[17] Lencrerot R, Litman A, Tortel H and Geffrin J-M 2009 Imposing Zernike representation for imaging two-dimensional targets *Inverse Probl.* **25** 035012 (21pp)
[18] van den Berg P M and Kleinman R E 1997 A contrast source inversion method *Inverse Probl.* **13** 1607–20
[19] Abubakar A, van den Berg P M and Habashy T M 2005 Application of the multiplicative regularized contrast source inversion method on TM- and TE-polarized experimental fresnel data *Inverse Probl.* **21** S5–13
[20] Bloemenkamp R F, Abubakar A and van den Berg P M 2001 Inversion of experimental multi-frequency data using the contrast source inversion method *Inverse Probl.* **17** 1611–22
[21] Abubakar A, Hu W, van den Berg P M and Habashy T M 2008 A finite-difference contrast source inversion method *Inverse Probl.* **24** 065004 (17pp)
[22] Abubakar A and van den Berg P M 2004 Iterative forward and inverse algorithms based on domain integral equations for three–dimensional electric and magnetic objects *J. Comput. Phys.* **195** 236–62
[23] Collin R E 1991 *Field Theory of Guided Waves* (New York: IEEE Press)
[24] Mojabi P and LoVetri J 2009 Overview and classification of some regularization techniques for the Gauss–Newton inversion method applied to inverse scattering problems *IEEE Trans. Antennas Propag.* **57** 2658–65
[25] Kilmer M E and O'leary D P 2001 Choosing regularization parameters in iterative methods for ill-posed problems *SIAM J. Matrix Anal. Appl.* **22** 1204–21
[26] Chung J, Nagy J G and O'leary D P 2008 A weighted-GCV method for Lanczos-hybrid regularization *Electron. Trans. Numer. Anal.* **28** 149–67
[27] van den Berg P M 2001 Nonlinear scalar inverse scattering: algorithms and applications *Scattering and Inverse Scattering in Pure and Applied Sciences* vol 1 ed E R Pike and P C Sabatier (London: Academic) pp 121–41
[28] Brandwood D H 1983 A complex gradient operator and its application in adaptive array theory *IEE Proc. F and H* **130** 11–6
[29] van den Bos A 1994 Complex gradient and Hessian *IEE Proc., Vis. Image Signal Process.* **141** 380–3
[30] Li H and Adaly T 2008 Complex-valued adaptive signal processing using nonlinear functions *EURASIP J. Adv. Signal Process.*
[31] Bjork A 1996 *Numerical Methods for Least Squares Problems* (Philadelphia: SIAM)
[32] Abubakar A, van den Berg P M and Semenov S Y 2004 A robust iterative method for Born inversion *IEEE Trans. Geosci. Remote Sens.* **42** 342–54
[33] van den Berg P M, van Broekhoven A L and Abubakar A 1999 Extended contrast source inversion *Inverse Probl.* **15** 1325–44
[34] Kooij B J and van den Berg P M 1998 Nonlinear inversion in TE scattering *IEEE Trans. Microw. Theory Tech.* **46** 1704–12
[35] Belkebir K and Saillard M 2001 Special section: testing inversion algorithm against experimental data *Inverse Probl.* **17** 1565–71
[36] Geffrin J-M, Sabouroux P and Eyraud C 2005 Free space experimental scattering database continuation: experimental set-up and measurement precision *Inverse Probl.* **21** S117–30
[37] Paulsen K D and Meaney P M 1999 Nonactive antenna compensation for fixed-array microwave imaging. I. model development *IEEE Trans. Med. Imag.* **18** 496–507